10.1002/anie.202416960

WILEY-VCH

RESEARCH ARTICLE

On the Origin of Capacity Increase in Rechargeable Magnesium Batteries with Manganese Oxide Cathodes and Copper Metal Current Collectors

Zhao Li,[+,a,b] Yi Li,[+,b, d] Yang Zhan,[a] Xiaodong Lin,*[b] Yingying Yao,[a] Tianshuo Zhao,[a] Fengzhan Sun,[a] Hao Xu,[a] Zhewen Ma,[c] Wei Zhang,[e] Yanling Xue,[e] Xiaolong Li,[e] Alexandru Vlad,*[b] Jianxin Zou*[a]

[a] National Engineering Research Center of Light Alloy Net Forming, State Key Laboratory of Metal Matrix Composite, Center of Hydrogen Science, School of Materials Science and Engineering, Shanghai Jiao Tong University, Shanghai 200240, China.
[b] Institute of Condensed Matter and Nanosciences, Université Catholique de Louvain, Louvain-la-Neuve B-1348, Belgium.
[c] State Key Laboratory of Advanced Processing and Recycling of Nonferrous Metals, School of Materials Science and Engineering, Lanzhou University of Technology, Lanzhou, 730050, China.
[d] Institute for Clean Energy & Advanced Materials, School of Materials and Energy, Southwest University, Chongqing 400715, China.
[e] Shanghai Synchrotron Radiation Facility, Shanghai Advanced Research Institute, Chinese Academy of Sciences, Shanghai 201204, China.
[+] These authors contributed equally to this work.
* Correspondence e-mail: xiaodong.lin@uclouvain.be; alexandru.vlad@uclouvain.be; zoujx@sjtu.edu.cn

Abstract: Rechargeable magnesium batteries (RMBs), with Cu as positive electrode current collector (CC), typically display a gradual capacity increase with cycling. Whereas the origin of this was suggested in gradual active material electro-activation, the fact that this is prevalent in many positive electrode material systems remains unexplained. Herein, we elucidate the underlying mechanism through a series of multiscale joint operando X-ray characterizations, including operando synchrotron X-ray diffraction and imaging technology. We select a series of manganese oxides as benchmark positive electrodes and find that no magnesium ions are stored within the lattices of these materials, despite an apparent cell capacity increase with cycling. The origin of capacity increase is rooted in the gradual electrochemical corrosion of metallic Cu, release of Cu(I, II) species in electrolyte, and their subsequent redox activity, resulting in apparent electrode capacity gains. Furthermore, the shuttle and redox speciation of Cu ions trigger the irreversible depletion of both the Cu CC (or any other source) and the magnesium metal, ultimately leading to cell failure. Our work suggests the need to reconsider the appropriateness of using Cu as a positive electrode CC for RMBs.

Introduction

In alkali metal battery systems, the voltage-capacity profile is a crucial indicator of electrochemical performance, as any electrochemical redox reaction involving metal ions within the electrodes can be tracked by changes in current and voltage in the external circuit.[1] Research on various battery systems has nevertheless demonstrated that directly assessing battery performance using these test results is not entirely reliable.[2] Side reactions within the battery system can produce performance artifacts, leading to misinterpretations of battery performance and impeding further development and application of these cell chemistries.[2] For instance, in lithium-oxygen batteries, the capacity observed during charging often results from the oxidative decomposition of the byproducts such as lithium carbonate or the electrolyte, rather than from the desired product of lithium peroxide.[2a, 2b] In sulfide all-solid-state batteries, the high reversible specific capacity during charging and discharging is likely partly due to the reversible redox reaction of the sulfide electrolyte.[2c, 2d] In calcium-metal batteries, the capacity during charge-discharge cycles is not necessarily related to the insertion/de-insertion of calcium ions but rather to electrolyte-related side reactions.[2e, 2f] Therefore, accurately assessing battery performance requires meticulous investigation of the electrochemical redox mechanism behind the voltage-capacity profile response using advanced characterization techniques.

There are likewise intriguing yet poorly understood phenomena in rechargeable magnesium battery (RMB) systems. For example, in sulfur/selenium or metal sulfide/selenide positive electrode systems, using a Cu foil (or any other Cu ion source) instead of the conventional aluminum, carbon, or stainless-steel as current collector (CC) results in an initial capacity increase followed by decay, contrary to the conventional trend of expected capacity decay (Fig. 1).[3] Most studies simply attribute this to an electrochemical activation process of the active material.[4] However, it is worth noting that the anodic stability of metallic Cu is below 1.8 V (vs. Mg/Mg^{2+}),[5] while the charging voltage of many RMB positive electrode materials often exceeds this threshold.[3a, 6] Consequently, continuous corrosion and consumption of Cu(0) is expected, along with potential interference from soluble Cu(I, II) species with the active material electrode constituents. For instance, soluble Cu(I, II) species may participate in electrochemical redox reactions, contributing to a portion of the battery capacity. This may result in the performance artifacts of an apparent initial increase in Mg storage capacity.

The introduction of Li ions into the Mg-ion electrolyte also presents an interesting phenomenon of significant capacity enhancement in RMBs.[7] Some studies have shown that lithium ions promote the magnesiation/de-magnesiation kinetics, thereby enhancing the storage capacity of Mg ions.[7c–e] However, it is possible that in some systems, Li ions merely contribute to the

10.1002/anie.202416960

capacity through lithiation/de-lithiation reactions without enhancing Mg ion storage, as not all studies provide evidence that Li ions promote the Mg storage. Therefore, the electrochemical performance of RMBs using Cu as a positive electrode CC or introducing Li ions into the electrolyte needs careful and comprehensive evaluation to avoid misinterpretation of battery performance due to artifacts induced by other electrochemical redox reactions unrelated to Mg ion storage.

In this work, we study the Mg storage artifacts induced by using Cu as a positive electrode CC or introducing Li ions into the all-phenyl complex (APC) electrolyte in manganese oxide (Mn_xO_y) cathode-based RMBs. Careful experiment design and cell construct reveals that no effective Mg-ion storage takes place in the studied five types of Mn_xO_y material systems. When these materials are deposited on Cu CC, all systems display a steady increase in capacity as cycling progresses, with similar behavior also noted for Li and Mg ions mixed electrolyte (APC-Li^+). We show that the capacity increase with Cu as CC is due to the gradual electrochemical corrosion of metallic Cu during anodic polarization, release of Cu(I, II) species into the electrolyte, leading to a cascade of redox at both electrodes and within the bulk electrolyte. These processes are enhanced throughout the cycling process, leading to a gradual increase in capacity. The capacity gain in the APC-Li^+ electrolyte is additionally enhanced by the lithiation/de-lithiation reaction of the Mn_xO_y material rather than Mg storage. We also show the shuttling effect of the generated soluble Cu species, where ions migrate toward the Mg metal electrode and undergo reduction with the formation of Cu metal deposits, causing irreversible depletion of the Mg metal and ultimately leading to battery failure. This study highlights the need for caution in the study of RMBs, as capacity increases due to Cu CC or Li ions in the electrolyte may be artifacts rather than true enhancements of Mg-ion storage ability.

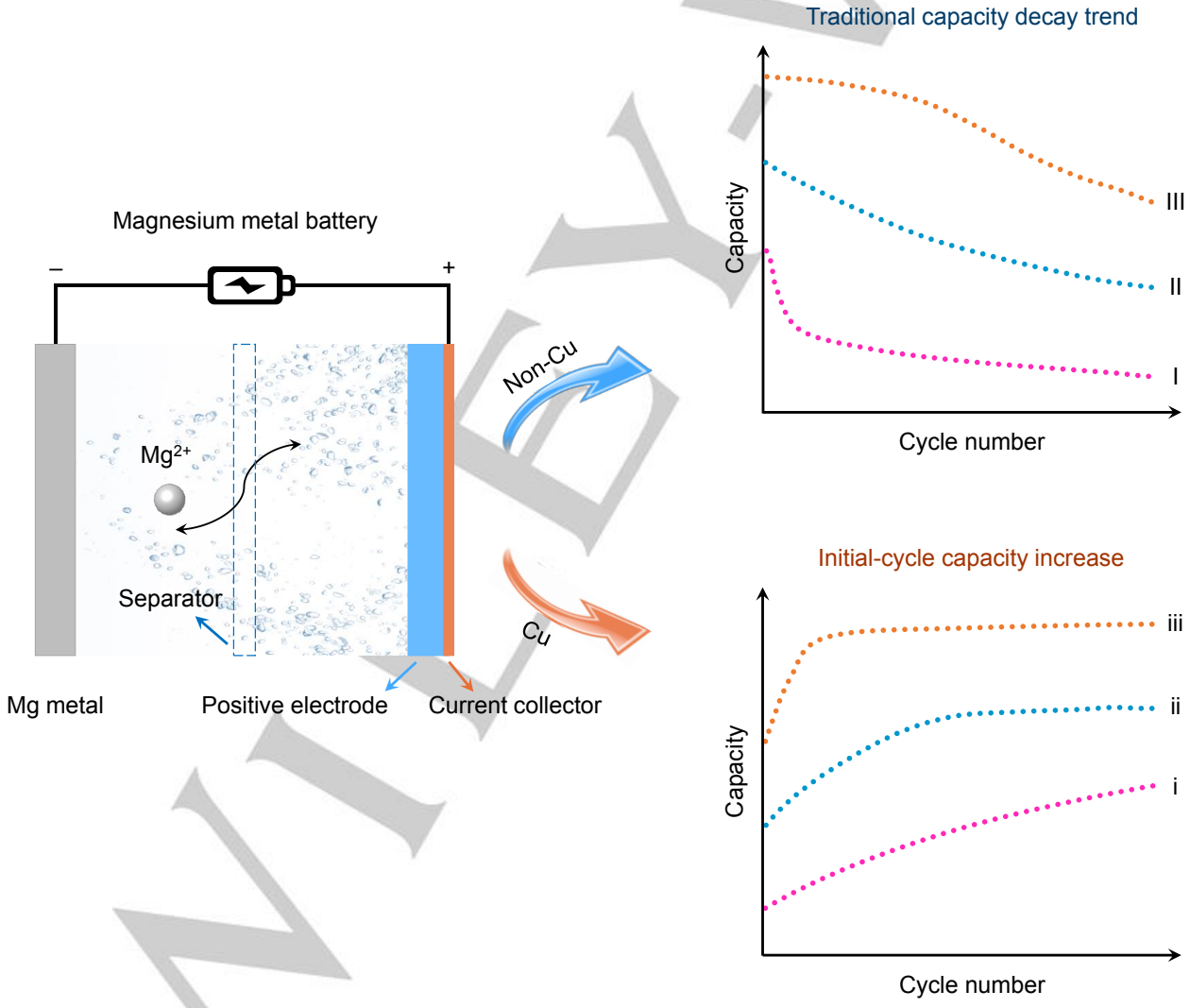

Figure 1. Relationship between the design and composition of an RMB system and its cycling capacity retention. The schematics propose that the nature of the CC affects the cycling capacity evolution of RMBs. When metallic Cu elements are present (bottom-right panel), the capacity appears to increase steadily over the initial cycles (monotonic, or step-wise behavior). Whereas if no metallic Cu elements are being used in the cell construct (top-right panel), the initial and subsequent cycling is characterized by conventional capacity fade.

Results and Discussion

Is there Mg-ion storage in MnO, Mn_2O_3, Mn_3O_4, and β-MnO_2 phases?

In this study, we selected five Mn_xO_y-based positive electrode material systems (Figs. S1 and S2): MnO, Mn_2O_3, Mn_3O_4, β-MnO_2, and MnO/reduced graphene oxide composite (MnO/rGO) as the research focus for several reasons: (1) Previous studies have shown that positive electrode material systems such as sulfur/selenium or metal sulfide/selenide chemically react with the Cu CC during cycling, producing species like CuS_x/$CuSe_x$, which complicates the study of reaction mechanisms.[3,4,8] To avoid this interference in analyzing the influence of Cu CC on Mg storage performance and mechanisms, we chose an oxide system that is chemically inert with the Cu CC. (2) Mn_xO_y materials (*e.g.* Mn_2O_3, Mn_3O_4, MnO_2) are one of the most widely studied oxide systems in RMBs and have been reported for Mg ion storage, making them representative of oxide systems (refer to Table S1). (3) Previous studies on Mn_xO_y for Mg-ion storage involved materials synthesis through carefully designed experimental methods, which may impart unique characteristics (refer to Table S1). Since Mn_xO_y materials have long been commercialized, they are inexpensive and readily available. Using such systems not only enhance data reproducibility but also allows for the investigation of their universal applicability in Mg-ion storage. Finally, MnO has not yet been explored as a positive electrode material in RMB systems, making it particularly interesting to study its Mg storage properties and compare them with those of other Mn_xO_y materials.

It is well known that APC electrolyte exhibits more highly reversible Mg plating/stripping behavior compared to other electrolyte systems. Therefore, we selected APC as the electrolyte to minimize interference from Mg-metal issues in this study.[9] Figures 2a, 2d, 2e and S3–S7 illustrate the electrochemical performances of the Mn_xO_y-based RMBs using Cu as the positive electrode CC with a 0.4 M APC electrolyte formulation. The first observation is that the initial discharge capacity of all cells is negligibly low (in the range of 0 ~ 0.64 mAh g^{-1}, or 0 ~ 0.005 mAh cm^{-2}). Subsequently, in all systems, the capacity was found to gradually increase with the extent of cycling. For example, the discharge capacity of the Mg | APC | MnO-Cu cell markedly increased to 75 mAh g^{-1} after 50 cycles. This phenomenon is similar to the initial-cycle capacity increase process observed in Mg-sulfur/selenium and Mg-metal sulfide/selenide systems.[3,4,8] In contrast, the RMBs using graphite paper (denoted as G in the following text) as the positive electrode CC did not display the initial-cycle capacity increase process (Figs. 2b and S8–S11) with all other parameters kept identical. No charge/discharge plateaus were observed, and only double-layer capacitance characteristics were evident even after 800 cycles in the Mg | APC | MnO-G cell configuration (Figs. 2b

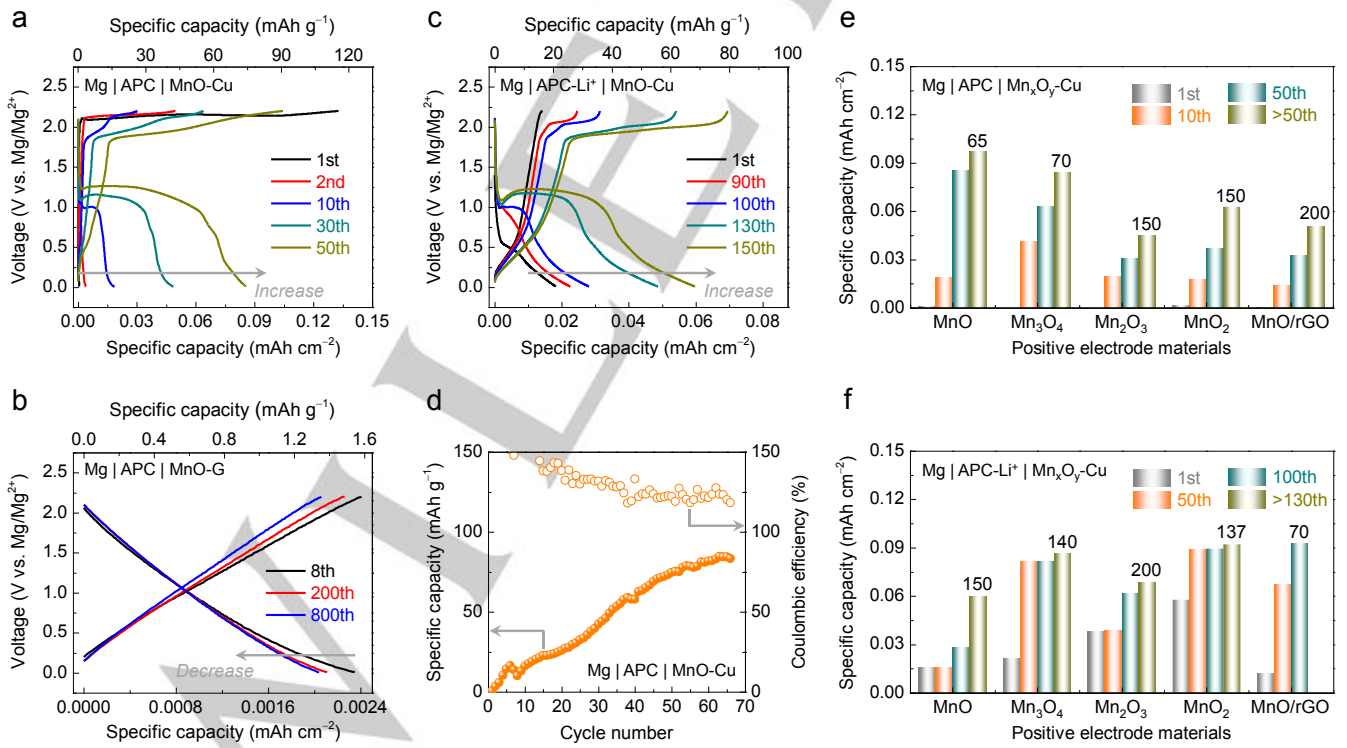

Figure 2. Electrochemical performance analysis of RMBs in the presence or absence of Cu metal elements in the positive electrode construct. (a, b, c) Galvanostatic charge-discharge profiles and (d) the specific discharge capacity and Coulombic efficiency of the RMBs using MnO as the positive electrode material, and using Cu (a, c, d) or graphite paper (b) as CC. The electrolyte used is APC in (a, b, d) and APC-Li^+ in (c). In all tests, a current density of 0.1 mA cm^{-2} was applied, and the voltage window was set to 0.01–2.2 V (vs. Mg/Mg^{2+}). Comparison of the specific discharge capacity at different cycle indexes of the studied Mn_xO_y materials in RMBs comprising Cu metal in APC (e) and APC-Li^+ (f) electrolytes.

10.1002/anie.202416960

RESEARCH ARTICLE

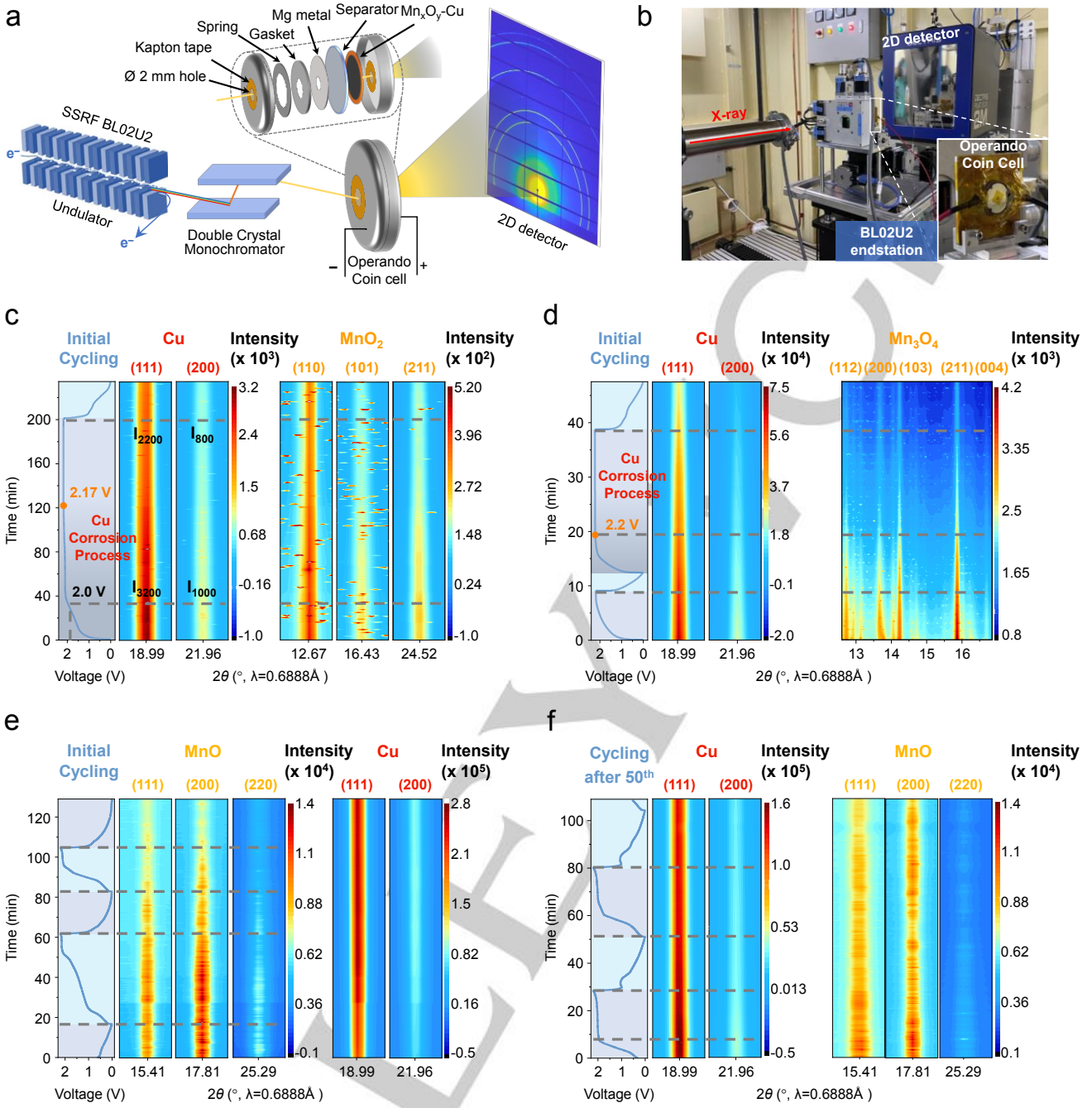

Figure 3. Operando synchrotron XRD. (a, b) Schematic and picture of operando synchrotron XRD devices. (c–f) Operando XRD contour maps and the corresponding 1st cycle discharge/charge profile of (c) MnO_2-Cu and (d) Mn_3O_4-Cu electrodes in APC electrolyte, and of MnO-Cu electrodes at the initial (e) cycles and (f) after 50 cycles in APC-Li^+ electrolyte.

and S8). This analysis indicates that the Mn_xO_y-based RMBs become efficient in storage only when using Cu as a positive electrode CC, which is unusual. Another interesting observation is with Li ions included into the APC electrolyte, all RMB systems demonstrate higher initial discharge capacity compared to the equivalent cells utilizing pure APC (refer to Figs. 2c, f and S12–S17). For instance, both the Mg | APC-Li^+ | MnO-Cu (Figs. 2c and S12) and Mg | APC-Li^+ | MnO-G (Fig. S17) cells manifested an initial discharge capacity of approximately 20 mAh g^{-1}. These outcomes again seem to imply that the introduction of Li ions into the electrolyte can promote the Mg ion storage performance.

To further investigate the capacity enhancement in Mn_xO_y-based RMBs using Cu as a positive electrode CC and introducing Li ions into the electrolyte, we employed operando synchrotron X-ray diffraction (XRD) technique[10] (Figs. 3a and 3b) to monitor the evolution of material structure and species throughout battery cycling. Figures 3c, 3d, and S18 display the operando XRD patterns of MnO_2-Cu, Mn_3O_4-Cu and Mn_2O_3-Cu based RMBs with APC electrolyte. Unexpectedly, no evidences of Mg ion storage were observed, such as shifts in the diffraction peak positions due to ion insertion, or the formation of new phases (e.g., Mn and MgO) due to conversion reactions. Conversely, a decrease in the

intensity of the Cu diffraction peaks during continuous charging and discharging cycles was observed in all systems. Taken the MnO_2-Cu system as an example, the intensity of the Cu diffraction peak slightly decreased when the initial charge potential exceeded 2.0 V. However, upon prolonged overcharging, a substantial decrease in the Cu diffraction peak intensities was observed (e.g., Cu(111) peak intensity decreased from 3200 to 2200 photon counts, and the Cu(200) peak from 1000 to 800 photon counts). It is worth mentioning that the discharge capacity gradually increased with continued cycling as well, as previously discussed. Additionally, similar behavior was observed in the Mg | APC-Li^+ | Mn_xO_y-Cu system (Figs. 3e, f and S19–22), with no evidences of Mg storage found during cell cycling. The joint results of electrochemical analyses and operando synchrotron XRD results reveal that the capacity gain in the studied RMBs originates from factors other than Mg-ion storage in Mn_xO_y materials. Specifically, it is likely due to the corrosion of metallic Cu and the storage of Li ions (in the case of APC and APC-Li^+ electrolytes).

Cu corrosion and the effect on RMB cycling.

To evidence the role of the Cu corrosion and subsequent redox reactions in RMBs over long-term charging and discharging periods, we selected a simplified model system and cell construct, the Mg | APC | Cu cell. No active material was used, implying no Mg-ion storage would take place, thus normally no storage capacities should be observed. Additionally, to prevent the results from potential interference due to stainless steel corrosion at high voltages using the APC electrolyte, we designed a Swagelok-type cell (illustrated in the inset of Fig. 4a), comprising a polytetrafluoroethylene body and two molybdenum caps. Figures 4a and 4b illustrate the cyclic voltammetry (CV) curves of the Mg | APC | Cu cell within the potential range of 0.001 to 2.2 V (vs. Mg/Mg^{2+}) at a scan rate of 0.1 mV s^{-1}. In the initial cathodic scan, no distinct redox process could be noted (orange curve in Figs. 4a and 4b). During the subsequent anodic scan, a well-defined redox peak emerged at 2.0 V (orange curve in Figs. 4a and 4b), corresponding to the electrochemical oxidation of Cu to Cu^+ (Equation (1), refer to Fig. S23). To be noted that the charge plateaus in the Mn_xO_y RMBs (Figs. 2a and 2c) are also located at around 2 V (vs. Mg/Mg^{2+}). The generated Cu^+ is however unstable and will disproportionate into metallic Cu and Cu^{2+} ions (Equation (2)). Consequently, in the second cathodic scan (blue curve in Figs. 4a and 4b), no reduction of Cu^+ near 2.0 V is noted (Equation (3)), while a reduction peak is observed at 0.6 V, corresponding to the reduction of Cu^{2+} to Cu^0 (Equation (4)) or to Cu^+ (Equation (5)). On the second anodic cycle, no oxidation of Cu^+ could be noted (around 0.6 V, Equation (6)), whereas a new oxidation peak emerged at 1.7 V, corresponding to the direct two-electron oxidation of Cu (Equation (7)), corresponding to the reverse process of Equation (4). Since Equation (4) and Equation (7) involve a direct two-electron reduction/oxidation process of Cu^{2+}/Cu, the kinetics is slow, resulting in widely spaced and relatively poorly reversible redox peaks.

It has to be noted that the anodic current at potentials of 2.0 V and above progressively increased upon continuous cycling (Figs. 4a and 4b), indicating enhanced corrosion of the metallic Cu CC. According to Equations (1–7), Cu^{2+} ions remain in the electrolyte at the end of each CV scan cycle, while also considering diffusion away from the Cu electrode surface given the slow cycling conditions applied. Consequently, as the scanning cycles advance and the corrosion of the Cu intensifies, an accumulation of Cu^{2+} ion occurs in the electrolyte. According to Le Chatelier principle, an excessive presence of Cu^{2+} ions in the electrolyte may adversely impact Equation (2). Consequently, some Cu^+ ions may coexist in the electrolyte, as evidenced by the CV curves after numerous cycles (refer to Figs. 4a and 4b). Taking the 30th CV scan as an example (Fig. 4b), a new reduction peak is visible near 1.1 V during the cathodic scan, corresponding to the reduction reaction of Cu^+ (Equation (3)). Additionally, the reduction peak near 0.6 V is split into two peaks, with the higher potential peak representing the direct reduction of Cu^{2+} to metallic Cu (Equation (4), refer to Fig. S23), and the slightly lower potential indicating the reduction of Cu^{2+} to Cu^+ (Equation (5), refer to Fig. S23). Correspondingly, the new oxidation peak observed near 1.0 V in the anodic scan would correspond to the oxidation of Cu^+ to Cu^{2+} ions (Equation (6)). It is worth mentioning that the reduction peak A1 in the range of 0.01−0.4 V in Fig. 4b may be related to the underpotential deposition of Mg or the reduction of solvent and salts, and accordingly, the oxidation peak A1' near 0.5 V may be the associated inverse process. The above phenomena provide evidence that electrochemical redox reactions involving Cu^+ begin to occur in the electrolyte as the scanning cycle progresses.

Upon elevating the voltage scan limit from 2.2 to 2.5 V (Figs. 4c, S24 and S25), the oxidative corrosion of Cu intensified, eventually leading to cell failure due to intense corrosion and depletion of Cu metal. As illustrated in Figs. S24, 4c and 4d, after 10 and 500 cycles at scan rates of 0.1 and 10 mV s^{-1}, respectively, the Cu foils display signs of severe corrosion. Additionally, Cu deposits were observed on the separator surfaces facing both the positive and negative electrodes, as well as on the Mg metal surface. The Cu deposits on the separator facing the negative electrode side and the Mg metal surface are attributed to the reduction of Cu ions shuttling to the negative electrode (Equations (3) and (4)). Whereas the Cu deposits on the separator's positive electrode side primarily result from the chemical disproportionation of Cu^+ (Equation (2)).

Figures 4e and 4f illustrate the galvanostatic discharge-charge profiles and cycling stability of Mg | APC | Cu cells, conducted within the voltage range of 0.001–2.2 V and at a current density of 0.1 mA cm^{-2}, respectively. Corroborating the CV data analysis, this cell also manifests the initial-cycle capacity increase, akin to the observed behavior in Mn_xO_y-Cu electrode systems. Furthermore, both Mg | APC | Cu and Mg | APC | Mn_xO_y-Cu cells exhibit distinctive and similar electrochemical redox characteristics, that are assigned to Cu^{2+} and Cu^+ redox processes (as evidenced by the dQ/dV plot analysis, Figs. S26 and 27) further supporting the inactive nature of Mn_xO_y for Mg storage. These reaffirm that the cycling capacity increase process

10.1002/anie.202416960
WILEY-VCH

RESEARCH ARTICLE

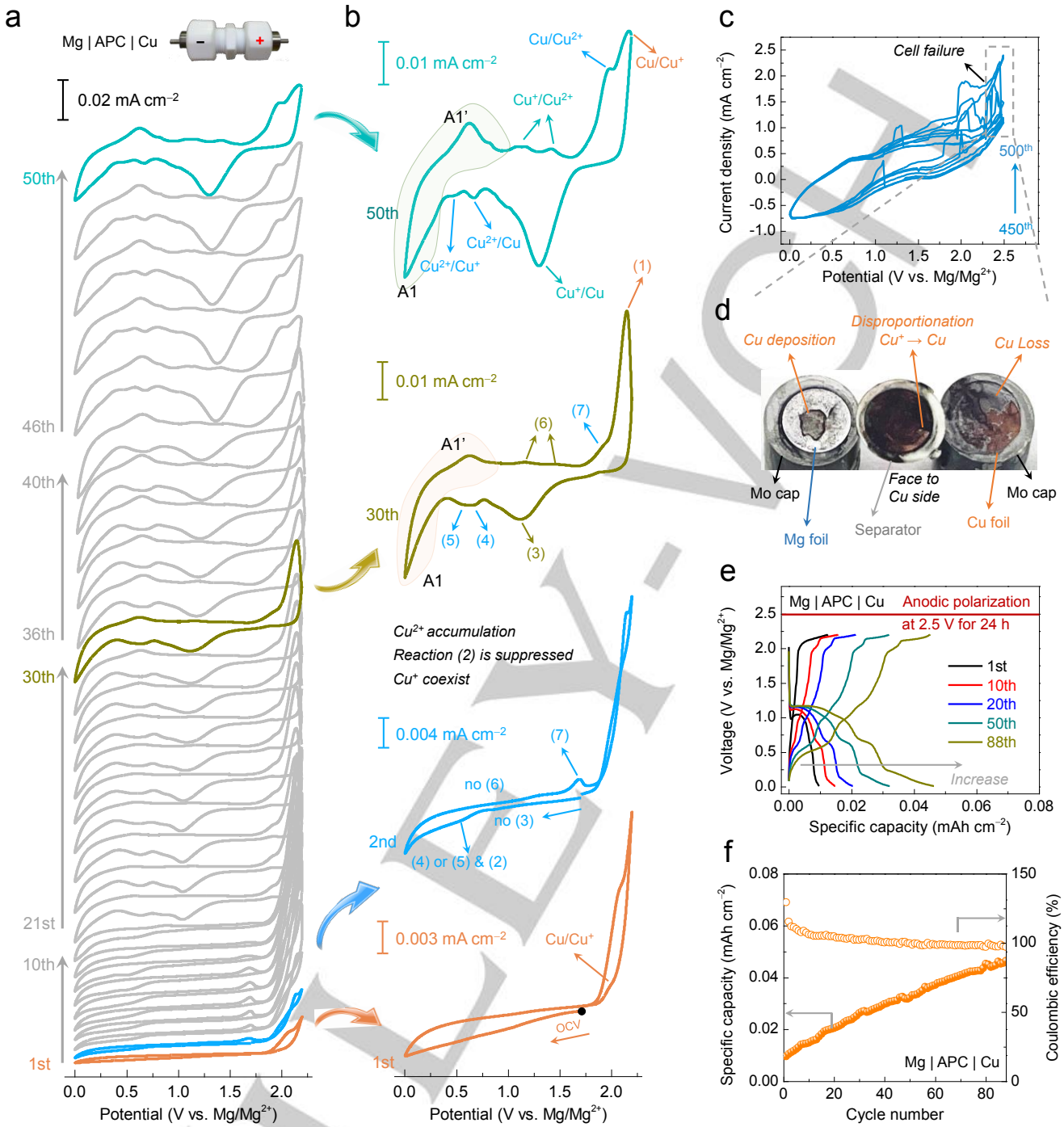

Figure 4. Redox chemistry of Cu species in non-aqueous APC electrolytes. (a–c) CV curves of the Mg | APC | Cu cell at a scan rate of (a, b) 0.1 or (c) 10 mV s^{-1} with potential ranges of (a, b) 0.001–2.2 V and (c) 0.001–2.5 V. (d) Optical photograph of Cu electrode, separator and Mg electrode extracted from the Mg | APC | Cu cell after 500 CV cycles at a scan rate of 10 mV s^{-1} as shown in Fig. 4c. (e, f) Galvanostatic charge-discharge profiles (e) and specific discharge capacity and Coulombic efficiency (f) of the Mg | APC | Cu cell at a current density of 0.1 mA cm^{-2} and in a voltage window of 0.01–2.2 V. The data was recorded after charging at a constant voltage of 2.5 V for 24 h.

in the RMBs containing metallic Cu constituents primarily stems from the electrochemical redox of the Cu species, rather than from the intrinsic storage action process within the Mn_xO_y active materials.

$$Cu \rightarrow Cu^+ + e^- \quad (1)$$

$$2Cu^+ \rightarrow Cu + Cu^{2+} \quad (2)$$

$$Cu^+ + e^- \rightarrow Cu \quad (3)$$

$$Cu^{2+} + 2e^- \rightarrow Cu \quad (4)$$

$$Cu^{2+} + e^- \rightarrow Cu^+ \quad (5)$$

$$Cu^+ \rightarrow Cu^{2+} + e^- \quad (6)$$

$$Cu \rightarrow Cu^{2+} + 2e^- \quad (7)$$

10.1002/anie.202416960

RESEARCH ARTICLE

To further illustrate that the irreversible depletion of Cu is responsible for the capacity increase and ultimately leading to cell failure, we observed the morphological changes in the electrodes and separator during the operation of Mg | APC | Cu cell utilizing operando synchrotron X-ray imaging technology[11] (Figs. 5a, 5b, S28 and S29). As depicted in Fig. 5c, the Mg negative electrode, glass fiber separator, and Cu positive electrode exhibited varying brightness levels owing to their distinct X-ray absorption characteristics. Upon anodic polarization at 2.5 V, the initial white contrast of the separator adjacent to the Cu positive electrode gradually darkened. This intensified with the extent of corrosion of Cu, as evident from the comparison of X-ray images of the operando cell at different time lapses. Based on the results and discussions in the above section, this occurrence is attributed to the electrochemical oxidation corrosion of Cu in the APC electrolyte, leading to the partial diffusion of Cu^{+} ions into the separator (Equation (1)), which then undergoes chemical disproportionation to generate metallic Cu and Cu^{2+} (Equation (2)).

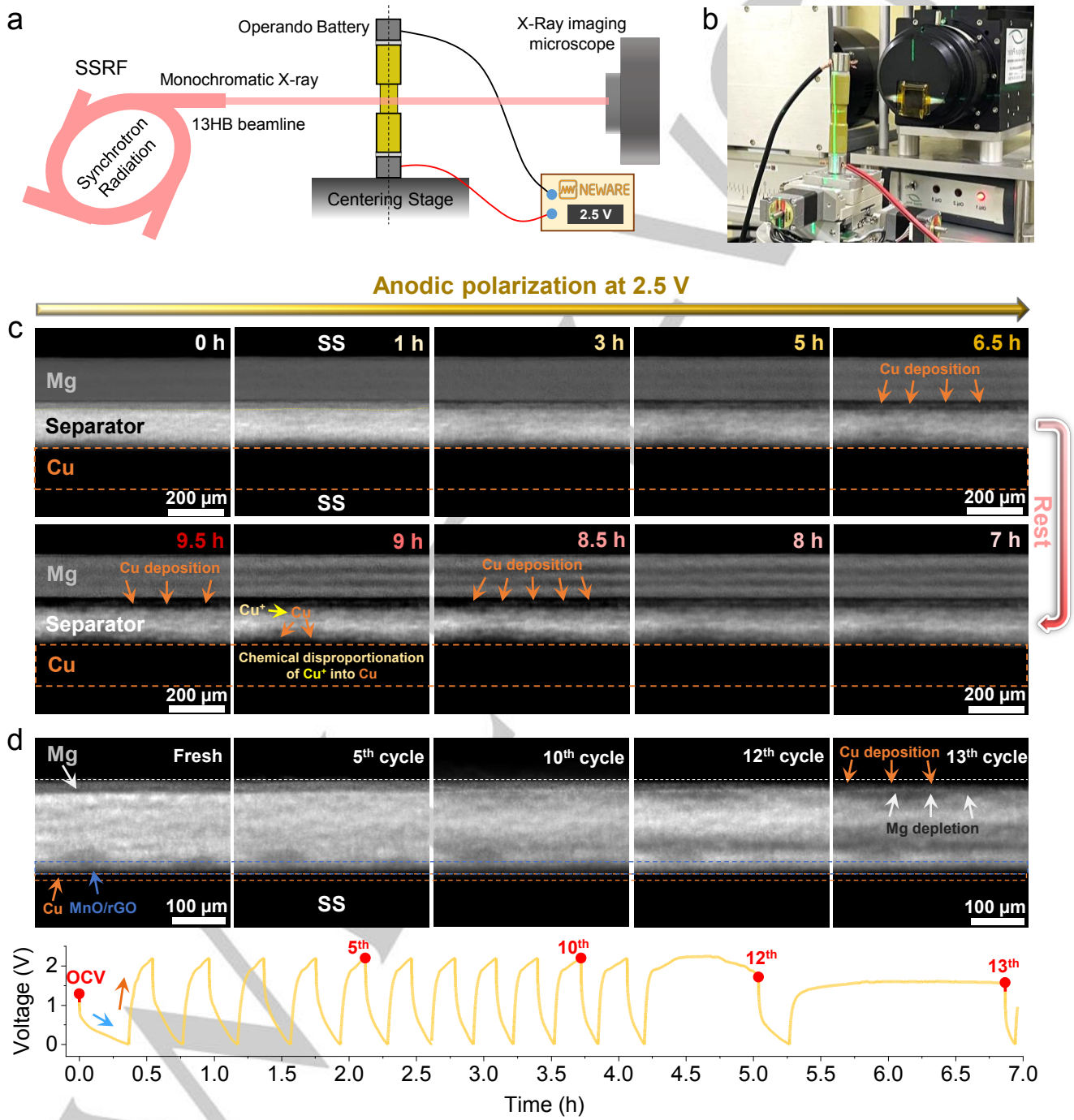

Figure 5. Operando synchrotron X-ray imaging. (a, b) Illustration and corresponding photograph of operando synchrotron X-ray imaging devices. (c) Real-time observation of the morphological evolution in the Mg | APC | Cu cell (using thick Cu and Mg foils) during potentiostatic charging at 2.5 V for 6.5 h, followed by a rest period for 3 h. (d) Operando synchrotron X-ray imaging measurement of the Mg | APC-Li^{+} | MnO/rGO-Cu cell (using thin Cu and Mg foils) during cycling, evidencing fast depletion of the Mg metal.

A significant accumulation of dark contrast material was also observed on the separator adjacent to the Mg negative electrode after 6.5 hours of polarization in the operando cell, consistent with the result depicted in the inset photograph of Figs. 4d and S24b. The respective dark deposits were identified as aggregates of Cu particles, also confirmed by SEM inspection (Fig. S30), energy-dispersive X-ray spectroscopy (EDS) mapping (Fig. S30), and XPS analysis (Fig. S31). The underlying process can be succinctly summarized to: Cu^{+} and/or Cu^{2+} ions diffuse through the separator toward the Mg negative electrode, are reduced in contact with Mg, leading to the formation of Cu through a displacement reaction (Equation (8) or Equation (9)). The monitoring was continued after the interruption of the applied voltage for another 3.5 h revealing that changes persisted even when the corrosion process was halted, as the dark contrast deposits on the separator side adjacent to the Mg negative electrode continued to increase during this period. The dissolved Cu^{+}/Cu^{2+} ions continue to diffuse toward the Mg negative electrode, reacting with Mg to generate Cu particles, being at the origin of the irreversible depletion of Mg metal in the cell. Given that the general practice is to use an excess of Mg metal as the negative electrode, the problem is being masked in many RMB systems. However, this will become critical in practical systems, as often lower negative to positive electrode capacity (N/P) ratio will be required.

$$2Cu^{+} + Mg \rightarrow 2Cu + Mg^{2+} \quad (8)$$

$$Cu^{2+} + Mg \rightarrow Cu + Mg^{2+} \quad (9)$$

To confirm that metallic Cu corrosion during cell cycling can additionally lead to the detachment of electrode material from the Cu CC, we conducted additional operando X-ray imaging on a RMB with an MnO/rGO-Cu composite electrode (Fig. S32). To accurately reflect the morphological changes of both the electrode and separator in actual battery tests, we reduced the thickness of the Mg metal and the Cu foils to the same dimensions used in the performance tests (Fig. S33). Notably, due to the low X-ray absorption contrast of the soft carbon element (C) in rGO, the imaging predominantly revealed the MnO nanoparticles coated on the Cu CC. As depicted in Fig. 5d, dark deposits progressively emerged on the Mg metal negative electrode surface with the extent of cycling, occurring from the reduction of Cu ions to metallic Cu at the Mg metal surface. Both the thickness of the Mg metal and of the MnO positive electrode material significantly decreased with the augmentation of dark contrast deposits – the aggregated Cu particles, as confirmed by SEM inspection, EDS mapping, and XPS analysis again (Figs. S34–S36). These outcomes confirm that Cu corrosion and redox will cause premature cell degradation and depletion of Cu CC and Mg metal negative electrode.

Outlook on the electrochemistry of RMBs containing Cu metal elements

As schematized in Fig. 6, since the oxidation potential of Cu is lower than 1.8 V (vs. Mg/Mg^{2+}),[5] any electrode material with an operating voltage window above 1.8 V (vs. Mg/Mg^{2+}) will trigger corrosion of Cu, which will result in electrochemical redox of Cu species and a gradual capacity increase phenomenon in the cell, as the mass of these Cu species is not included in the cell capacity calculation, thus the Cu redox reactions will contribute to an additional capacity. The higher the upper charging voltage is applied, the more significant will be the corrosion and faster the Cu redox will be detected (early cycles). Systems operating near or above 1.8 V may have a short period of time (i.e., fewer cycles) with lower corrosion and contribution of Cu redox, but as the operating time increases (e.g., extended cycling), Cu redox will gradually become significant. This, will raise a series of problems in the electrochemical cell, affecting the operation at all cell constituent levels: (1) corrosion and depletion of Cu CC; (2) shuttle of Cu-ions to negative electrode side, displacement, and depletion of Mg metal; (3) the irreversible depletion of the Cu CC will cause the detachment of the electrode material; (4) clogging

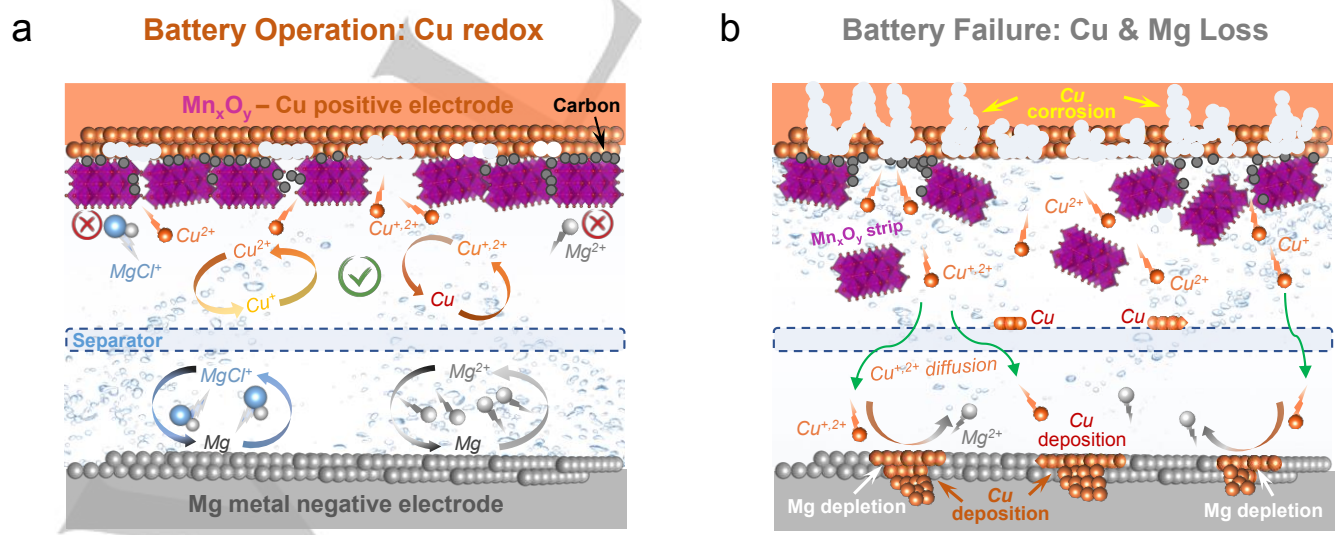

Figure 6. Schematics of the RMBs using metallic Cu elements. (a) Schematics of the electrochemical and chemical redox processes of Cu in an RMB. (b) Battery failure caused by irreversible depletion of the Cu CC, Mg metal and detachment of electrode materials.

of the separator, or creating metallic short-circuits with the metallic Cu from disproportionation of Cu(I) species. All of these are detrimental to the long-term cycling stability of RMBs and depending on the construct and the amounts of constituents in the cell (e.g. thickness of Cu and Mg foils, nature and amount of electrolyte), battery failure can be premature, or occur after an apparent capacity increase (Figs. S37 and 38). Regarding this last point, the calculation of the specific capacity of these RMB systems containing metallic Cu should also consider the mass of the Cu elements since these are part of the electrochemical redox during the cycling process and measured experimentally.

Conclusion

In summary, we analyze the behavior of RMBs using metallic Cu elements in the cell construct and uncover the origins of the observed occurrence of initial-cycle capacity increase. A series of positive electrode chemistries have been tested in combination with various CCs, and the apparent efficient Mg-storage is found to occur only in cells comprising metallic Cu elements (CC foil in this work). Through a comprehensive set of multi-scale joint operando synchrotron X-ray characterization techniques, we elucidate that this process primarily stems from the electrochemical corrosion of metallic Cu, followed by a series of redox processes of the dissolved in the electrolyte Cu (I) and Cu (II) species. With the extent of cycling, metallic Cu is detected within the separator and at the surface of Mg metal negative electrode. Altogether, these result in a series of processes that ultimately lead to cell failure. This work represents a significant advance in the mechanistic understanding of the redox chemistry of Cu CC and its implications for RMBs. This foundational comprehension is imperative for the future efficient design of cell configurations in the development of next-generation RMBs. Our investigation should raise awareness regarding the challenges and inadequacies associated with employing Cu as a positive electrode CC, paving the way for the standardization and normalization of cell configuration designs in RMBs.

Acknowledgements

Z. L. and Y. L. acknowledge the China Scholarship Council (CSC) for financial support. This work was also funded by the National Key Research and Development Program of China (No. 2022YFB3803700, 2022YFA1603901), the National Natural Science Foundation of China (Grant No. 12275344, 52171186), the Shanghai Technology Innovation Action Plan 2020-Integrated Circuit Technology Support Program (No. 20DZ1100602). This project received funding from the FWO and F.R.S.-FNRS under the Excellence of Science (EOS) program - ECOBAT [40007515] and partial support from European Research Council (ERC) under the European Union's Horizon 2020 research and innovation program (grant agreement No. 770870). The authors thank the staff from beamlines of BL02U2, BL13HB1 and User Experiment Assist System at the SSRF, and Wenjie Liu from Chinese Academy of Sciences for providing the used powder sample. Additionally, Z. L. acknowledges the CSC, and Wallonie-Bruxelles International (WBI) and the Fonds de la Recherche Scientifique (FNRS) for providing a joint scholarship (CSC-WBI-F.R.S.-FNRS), which is used to encourage Ph.D. students exchange between China and Wallonia-Brussels. X. L. acknowledges financial support from the Marie Skłodowska-Curie Actions (grant agreement No. 101064286) for his postdoctoral fellowship. Z. M. acknowledges financial support from the Hongliu Distinguished Young Talent Support Program of Lanzhou University of Technology (No.062403).

Conflict of interest

The authors declare no conflict of interest.

Keywords: Magnesium metal batteries; synchrotron X-ray characterizations; X-ray imaging, operando X-ray characterizations; copper current collector

[1] a) A. Van der Ven, J. Bhattacharya, A. A. Belak, *Acc. Chem. Res.* **2013**, *46*, 1216-1225; b) J. Muldoon, C. B. Bucur, T. Gregory, *Chem. Rev.* **2014**, *114*, 11683-11720; c) M. Winter, B. Barnett, K. Xu, *Chem. Rev.* **2018**, *118*, 11433-11456; d) Z. Li, Q. Li, A. Zhang, W. Wen, L. Wang, Z. Wang, J. Wang, S. Lu, X. Li, Z. Wang, *New J. Chem.* **2019**, *43*, 18943-18950; e) M. R. Palacin, P. Johansson, R. Dominko, B. Dlugatch, D. Aurbach, Z. Li, M. Fichtner, O. Lužanin, J. Bitenc, Z. Wei, C. Glaser, J. Janek, A. Fernández-Barquín, A. R. Mainar, O. Leonet, I. Urdampilleta, J. A. Blázquez, D. S. Tchitchekova, A. Ponrouch, P. Canepa, G. S. Gautam, R. S. R. G. Casilda, C. S. Martinez-Cisneros, N. U. Torres, A. Varez, J.-Y. Sanchez, K. V. Kravchyk, M. V. Kovalenko, A. A. Teck, H. Shiel, I. E. L. Stephens, M. P. Ryan, E. Zemlyanushin, S. Dsoke, R. Grieco, N. Patil, R. Marcilla, X. Gao, C. J. Carmalt, G. He, M.-M. Titirici, *Journal of Physics: Energy* **2024**, *6*, 031501.

[2] a) B. D. McCloskey, R. Scheffler, A. Speidel, D. S. Bethune, R. M. Shelby, A. C. Luntz, *J. Am. Chem. Soc.* **2011**, *133*, 18038-18041; b) M. M. Ottakam Thotiyl, S. A. Freunberger, Z. Peng, P. G. Bruce, *J. Am. Chem. Soc.* **2013**, *135*, 494-500; c) D. H. S. Tan, E. A. Wu, H. Nguyen, Z. Chen, M. A. T. Marple, J.-M. Doux, X. Wang, H. Yang, A. Banerjee, Y. S. Meng, *ACS Energy Lett.* **2019**, *4*, 2418-2427; d) T. K. Schwietert, V. A. Arszelewska, C. Wang, C. Yu, A. Vasileiadis, N. J. J. de Klerk, J. Hageman, T. Hupfer, I. Kerkamm, Y. Xu, E. van der Maas, E. M. Kelder, S. Ganapathy, M. Wagemaker, *Nat. Mater.* **2020**, *19*, 428-435; e) A. L. Lipson, D. L. Proffit, B. Pan, T. T. Fister, C. Liao, A. K. Burrell, J. T. Vaughey, B. J. Ingram, *J. Electrochem. Soc.* **2015**, *162*, A1574; f) A. P. Black, C. Frontera, A. Torres, M. Recio-Poo, P. Rozier, J. D. Forero-Saboya, F. Fauth, E. Urones-Garrote, M. E. Arroyo-de Dompablo, M. R. Palacín, *Energy Storage Mater.* **2022**, *47*, 354-364.

[3] a) J. Zhang, Z. Chang, Z. Zhang, A. Du, S. Dong, Z. Li, G. Li, G. Cui, *ACS Nano* **2021**, *15*, 15594-15624; b) R. Mohtadi, O. Tutusaus, T. S. Arthur, Z. Zhao-Karger, M. Fichtner, *Joule* **2021**, *5*, 581-617; c) A. Robba, M. Mežnar, A. Vizintin, J. Bitenc, J. Bobnar, I. Arčon, A. Randon-Vitanova, R. Dominko, *J. Power Sources* **2020**, *450*, 227672; d) X. Cheng, Z. Zhang, Q. Kong, Q. Zhang, T. Wang, S. Dong, L. Gu, X. Wang, J. Ma, P. Han, H.-j. Lin, C.-T. Chen, G. Cui, *Angew. Chem. Int. Ed.* **2020**, *59*, 11477-11482; e) X. Qu, A. Du, T. Wang, Q. Kong, G. Chen, Z. Zhang, J. Zhao, X. Liu, X. Zhou, S. Dong, G. Cui, *Angew. Chem. Int. Ed.* **2022**, *61*, e202204423.

[4] a) Z. Zhang, Z. Cui, L. Qiao, J. Guan, H. Xu, X. Wang, P. Hu, H. Du, S. Li, X. Zhou, S. Dong, Z. Liu, G. Cui, L. Chen, *Adv. Energy Mater.* **2017**, *7*, 1602055; b) Y. Shen, Y. Wang, Y. Miao, M. Yang, X. Zhao, X. Shen,

Adv. Mater. **2020**, *32*, 1905524; c) H. Chen, H. Xu, B. Li, Z. Li, K. Zhang, J. Zou, Z. Hu, R. M. Laine, *Appl. Surf. Sci.* **2022**, *598*, 153768; d) H. Xu, Y. Li, D. Zhu, Z. Li, F. Sun, W. Zhu, Y. Chen, J. Zhang, L. Ren, S. Zhang, J. Zou, R. M. Laine, *Adv. Energy Mater.* **2022**, *12*, 2201608; e) Y. Shen, Y. Wang, Y. Miao, Q. Li, X. Zhao, X. Shen, *Adv. Mater.* **2023**, *35*, 2208289.

[5] a) D. Lv, T. Xu, P. Saha, M. K. Datta, M. L. Gordin, A. Manivannan, P. N. Kumta, D. Wang, *J. Electrochem. Soc.* **2012**, *160*, A351-A355; b) Y. Cheng, T. Liu, Y. Shao, M. H. Engelhard, J. Liu, G. Li, *J. Mater. Chem. A* **2014**, *2*, 2473-2477; c) N. Y. Chen Qiang, Yang Jun, Kailibnuer Kerimu, Wang Jiulin, *Acta Phys. -Chim. Sin.* **2012**, *28*, 2625-2631.

[6] a) M. Mao, T. Gao, S. Hou, C. Wang, *Chem. Soc. Rev.* **2018**, *47*, 8804-8841; b) Z. Zhang, S. Dong, Z. Cui, A. Du, G. Li, G. Cui, *Small Methods* **2018**, *2*, 1800020.

[7] a) Y. Gofer, O. Chusid, H. Gizbar, Y. Viestfrid, H. E. Gottlieb, V. Marks, D. Aurbach, *Electrochem. Solid-State Lett.* **2006**, *9*, A257; b) H. D. Yoo, I. Shterenberg, Y. Gofer, R. E. Doe, C. C. Fischer, G. Ceder, D. Aurbach, *J. Electrochem. Soc.* **2014**, *161*, A410-A415; c) T. Gao, M. Noked, A. J. Pearse, E. Gillette, X. Fan, Y. Zhu, C. Luo, L. Suo, M. A. Schroeder, K. Xu, S. B. Lee, G. W. Rubloff, C. Wang, *J. Am. Chem. Soc.* **2015**, *137*, 12388-12393; d) Y. Wang, C. Wang, X. Yi, Y. Hu, L. Wang, L. Ma, G. Zhu, T. Chen, Z. Jin, *Energy Storage Mater.* **2019**, *23*, 741-748; e) H. Xu, X. Zhang, T. Xie, Z. Li, F. Sun, N. Zhang, H. Chen, Y. Zhu, X. Zou, C. Lu, J. Zou, R. M. Laine, *Energy Storage Mater.* **2022**, *46*, 583-593.

[8] Z. Zhang, B. Chen, H. Xu, Z. Cui, S. Dong, A. Du, J. Ma, Q. Wang, X. Zhou, G. Cui, *Adv. Funct. Mater.* **2018**, *28*, 1701718.

[9] a) O. Mizrahi, N. Amir, E. Pollak, O. Chusid, V. Marks, H. Gottlieb, L. Larush, E. Zinigrad, D. Aurbach, *J. Electrochem. Soc.* **2008**, *155*, A103; b) N. Pour, Y. Gofer, D. T. Major, D. Aurbach, *J. Am. Chem. Soc.* **2011**, *133*, 6270.

[10] a) Z. Li, Y. Li, X. Ren, Y. Zhao, Z. Ren, Z. Yao, W. Zhang, H. Xu, Z. Wang, N. Zhang, Y. Gu, X. Li, D. Zhu, J. Zou, *Small* **2023**, *19*, 2370311; b) Z. Li, Q. Li, A. Zhang, W. Wen, L. Wang, Z. Wang, J. Wang, S. Lu, X. Li, Z. Wang, *New J. Chem.* **2019**, *43*, 18943-18950.

[11] F. Tang, Z. Wu, C. Yang, M. Osenberg, A. Hilger, K. Dong, H. Markötter, I. Manke, F. Sun, L. Chen, G. Cui, *Small Methods* **2021**, *5*, 2100557.

10.1002/anie.202416960

WILEY-VCH

RESEARCH ARTICLE

Entry for the Table of Contents

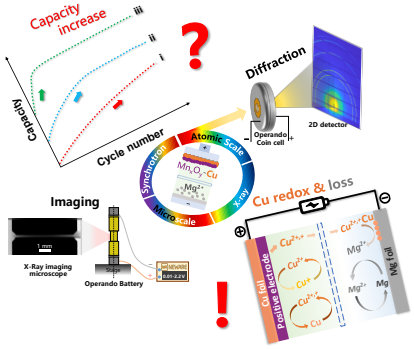

The capacity increase mechanism in rechargeable magnesium batteries featuring Cu metal is investigated through multiscale joint operando synchrotron X-ray characterizations. These analyses unveil that the capacity enhancement stems from the progressive electrochemical corrosion of metallic Cu. This corrosion initiates irreversible depletion of both the Cu current collector and magnesium metal, ultimately resulting in cell failure.